Optical Engineering 44(4), 000 (April 2005)

Aerosol ultraviolet absorption experiment (2002 to 2004), part 1: ultraviolet multifilter rotating shadowband radiometer calibration and intercomparison with CIMEL sunphotometers

Nickolay Krotkov
University of Maryland
Goddard Earth Sciences and Technology Center
Baltimore County, Maryland
E-mail: Krotkov@chescat.gsfc.nasa.gov

Pawan K. Bhartia
Jay Herman
NASA Goddard Space Flight Center
Greenbelt, Maryland

James Slusser, MEMBER SPIE
Colorado State University
Natural Resource Ecology Laboratory
U.S. Department of Agriculture
UV-B Monitoring and Research Network
Fort Collins, Colorado

Gordon Labow
Science Systems and Applications, Inc.
Lanham, Maryland 20706

Gwendolyn Scott
George Janson
Colorado State University
Natural Resource Ecology Laboratory
U.S. Department of Agriculture
UV-B Monitoring and Research Network
Fort Collins, Colorado

Thomas F. Eck
University of Maryland
Goddard Earth Sciences and Technology Center
Baltimore County, Maryland

Brent Holben
NASA Goddard Space Flight Center
Greenbelt, Maryland

Abstract. Radiative transfer calculations of UV irradiance from total ozone mapping spectrometer (TOMS) satellite data are frequently overestimated compared to ground-based measurements because of the presence of undetected absorbing aerosols in the planetary boundary layer. To reduce these uncertainties, an aerosol UV absorption closure experiment has been conducted at the National Aeronautics and Space Administration/Goddard Earth Sciences and Technology Center (NASA/GSFC) site in Greenbelt, Maryland, using 17 months of data from a shadowband radiometer [UV-multifilter rotating shadowband radiometer (UV-MFRSR), U.S. Department of Agriculture (USDA) UV-B Monitoring and Research Network] colocated with a group of three sun-sky CIMEL radiometers [rotating reference instruments of the NASA Aerosol Robotic Network (AERONET) network]. We describe an improved UV-MFRSR on-site calibration method augmented by AERONET-CIMEL measurements of aerosol extinction optical thickness (τ_a) interpolated or extrapolated to the UV-MFRSR wavelengths and measurement intervals. The estimated τ_a is used as input to a UV-MFRSR spectral-band model, along with independent column ozone and surface pressure measurements, to estimate zero air mass voltages V_0 in three longer wavelength UV-MFRSR channels (325, 332, 368 nm). Daily mean $\langle V_0 \rangle$, estimates and standard deviations are obtained for cloud-free conditions and compared with the on-site UV-MFRSR Langley plot calibration method. By repeating the calibrations on clear days, relatively good stability ($\pm 2\%$ in $\langle V_0 \rangle$) is found in summer, with larger relative changes in fall-winter seasons. The changes include systematic day-to-day $\langle V_0 \rangle$ decline for extended periods along with step jump changes after major precipitation periods (rain or snow) that affected the diffuser transmission. When daily $\langle V_0 \rangle$ values are used to calculate τ_a for individual 3-min UV-MFRSR measurements on the same days, the results compare well with interpolated AERONET τ_a measurements [at 368 nm most daily 1σ root mean square (rms) differences were within 0.01]. When intercalibrated against an AERONET sunphotometer, the UV-MFRSR is proven reliable to retrieve τ_a, and hence can be used to retrieve aerosol column absorption in the UV. The advantage of the shadowband technique is that the calibration obtained for direct-sun voltage can then be applied to diffuse-radiance voltage to obtain total and diffuse atmospheric transmittances. These transmittances, in combination with accurate τ_a data, provide the basis for estimating aerosol column absorption at many locations of the USDA UV-B Monitoring and Research network and for correction of satellite estimations of surface UV irradiance. [DOI: 10.1117/1.1886818]

Subject terms: ultraviolet radiation; aerosol absorption; CIMEL sunphotometer; AERONET network; ultraviolet multifilter rotating shadowband radiometer; diffuse fraction measurements; Langley calibration.

Paper UV-10 received Apr. 2, 2004; revised manuscript received Dec. 15, 2004; accepted for publication Jan. 14, 2005.

1 Introduction

Improved knowledge of aerosol absorption properties in the near UV is needed for modeling of tropospheric chemistry, because it affects the calculated rate of photolysis reactions,[1,2] smog production,[3] and as penetration of biologically harmful UV radiation to the surface.[4–17] Radiative transfer (RT) calculations show that decreases in UV due to moderate increases in absorbing aerosol amounts are comparable to that caused by stratospheric ozone recovery,[17] with one important difference. Aerosols affect both the UV-B (280- to 320-nm) and UV-A (320- to 400-nm) spec-

Fig. 1 UV-MFRSR shadowband radiometer, part of USDA UVMRP (left), and CIMEL sun/sky photometer, part of NASA AERONET network (right) were continuously run side by side at NASA GSFC in Greenbelt, Maryland (lat=39.03 deg N, long=76.88 deg W), in 2002 to 2004. The elevated location (the height of elevated platform at the roof of the building is ~20 m above ground and ~90 m above sea level) enables unobscured view of horizon by both instruments.

tral ranges, while ozone sensibly affects only the UV-B (at 310 nm, each 1% column ozone decrease produces approximately ~1% UV irradiance increase[4,6,17]). Therefore, local changes in aerosol amount or optical properties may enhance, reduce or even reverse UV radiation changes caused by expected stratospheric ozone recovery.[17] Although it is well known that iron oxides in desert dust[18–20] and soot produced by fossil fuel burning and urban transportation[21–23] strongly absorb UV radiation, properties of other potential UV absorbers, e.g., nitrated and aromatic aerosols,[5] are poorly known. Use of measurements from a shadowband radiometer[24–30] [the UV-multifilter rotating shadowband radiometer (UV-MFRSR), Yankee Environmental Systems, Turners Falls, Massachusetts] in both the UV-A and UV-B spectral regions enable separation of ozone absorption[31,32] and aerosol extinction and absorption effects[8,11–13] on surface UV irradiance. Since previous estimates of aerosol optical properties in the UV were sparse and not yet validated,[6–13] it was difficult to explain the observed discrepancy in modeled and measured UV irradiances[14–17] and photolysis rates.[1–5] The RT model discrepancy is a serious problem in satellite estimation of UV irradiance, even in cloud-free conditions.[14–17]

To reduce uncertainties in RT calculations of UV irradiance and actinic flux in cloud-free conditions, an aerosol UV absorption closure experiment has been conducted at the National Aeronautics and Space Administration, Goddard Earth Sciences and Technology Center (NASA/GSFC) site in Greenbelt, Maryland, using 17 months of data (2002 to 2004) from a shadowband radiometer [UV-MFRSR, U.S. Department of Agriculture (USDA) UV-B Monitoring and Research Network] colocated with a rotating group of three sun-sky CIMEL radiometers [reference instruments of NASA Aerosol Robotic Network (AERONET) network[33,34]]. This paper describes the UV-MFRSR on-site calibration and intercomparisons with AERONET measurements of aerosol extinction optical thickness[34] (τ_a). First, instrumentation and data sets used in this study are briefly described in Sec. 2. This is followed by a detailed description of the UV-MFRSR operating procedures, raw voltage corrections, and measurement uncertainties. The new on-site UV-MFRSR calibration technique was derived from comparisons with extrapolations and interpolations of AERONET τ_a, obtained by the CIMEL direct-sun technique and its Mauna Loa Langley calibration.[33,34] The technique and a spectral band model used to calibrate UV-MFRSR direct voltage measurements are discussed in Sec. 3, followed by analysis of the calibration results and comparisons with the Langley plot technique in Sec. 4. Long-term changes in the UV-MFRSR V_0 calibration observed at our site are discussed in Sec. 5. Finally, conclusions are given in Sec. 6, showing that the UV-MFRSR, when intercalibrated against an AERONET sunphotometer, was proven reliable to retrieve UV-A aerosol extinction optical thickness τ_a with accuracy better than 0.02 and hence can be used to infer the weak to moderate UV aerosol column absorption expected at relatively clean suburban Greenbelt site.[35] The inversion method and results of our aerosol absorption measurements are presented in a follow-up paper[36] (Part 2).

2 Instrumentation

The UV-MFRSR (Fig. 1, left) is a shadowband instrument that measures diffuse and total horizontal radiation.[26] The USDA UV-B Monitoring and Research Program (UVMRP) continuously operates 31 of these instruments at sites distributed across the United States.[24,25] These instruments are capable of retrieving column ozone,[31,32] aerosol optical thickness,[29] and calibrated diffuse and total UV irradiance.[24–30] A single measurement cycle consisted of measuring total horizontal irradiance (no sun blocking) following by three irradiance measurements with different positions of the shadowband blocking the sun and sky radiance on each side of the sun (at 9 deg from the center position). All spectral channels were measured within 1 s by seven separate solid state detectors with interference filters sharing a common Teflon diffuser.[26] The complete shadowing cycle takes ~10 s and was repeated every 3 min throughout the day without averaging of the data. The raw

data (voltages) were automatically transmitted every night (via dedicated telephone modem) to the USDA UVMRP processing center at the Colorado State University (Fort Collins) for calibration and further processing. The standard data processing included corrections of diffuse horizontal and direct-normal voltages based on National Oceanic and Atmospheric Administration (NOAA) Central Ultraviolet Calibrations Facility (CUCF) measured spectral and angular response functions and applied absolute radiometric (lamp) calibration to all irradiance components.[30] Subsequent monthly reprocessing included Langley on-site calibration checks on clear days using the Harrison and Michalsky algorithm[28,29] and calculation of the aerosol optical thickness and column ozone (all standard data available at http://uvb.nrel.colostate.edu/UVB/home_page.html). The standard calibration procedure differs from our experiments, where only cosine corrected voltages were used that were calibrated on-site against colocated AERONET sunphotometers measurements as described in the following.

Direct sun aerosol extinction optical thickness measurements were made with three CIMEL sun-sky radiometers (Fig. 1, right) that are reference instruments of the AERONET global network[33,34] (data available at http://aeronet.gsfc.nasa.gov). The automatic tracking sun- and sky-scanning radiometers make direct sun measurements with a 1.2-deg full field of view every 15 min at 340, 380, 440, 500, 675, 870, 940, and 1020 nm (nominal wavelengths). The measurements take 8 s to scan all eight wavelengths, with a motor-driven filter wheel positioning each filter in front of the detector. These solar extinction measurements were then used to compute aerosol extinction optical depth τ_a at each wavelength, except for the 940-nm channel, which was used to retrieve total precipitable water vapor. The filters utilized in the CIMEL instruments were ion-assisted deposition interference filters with a bandpass (full width at half maximum) of 2 nm for the 340-nm channel and 4 nm for the 380-nm channel, while the bandpasses of all other channels were 10 nm. The AERONET data were quality- and cloud-screened following the methodology of Smirnov et al.[37]

Ancillary measurements at our site included Brewer double monochromator column ozone measurements (Fig. 2) and surface pressure measurements from nearby USDA UVMRP Beltsville station corrected for the ~20-m altitude difference (Fig. 3).

3 UV-MFRSR Operating Procedures and Calibration

3.1 *UV-MFRSR Maintenance at GSFC Site*

One UV-MFRSR instrument from the USDA UVMRP network (head 271) was installed at the AERONET primary calibration site at NASA GSFC in Maryland, and routine operation of the instrument started on October 1, 2002. The instrument is located on an elevated rooftop platform that enables an unobstructed view of the horizon (Fig. 1). The UV-MFRSR internal head temperature was maintained close to 42 °C ($\langle T \rangle = 41.7$ °C, $\sigma_T = 0.22$ °C) and nighttime bias voltages were monitored throughout the deployment. A special bubble-level instrument was used to fine-tune the leveling to within 10 arcmin. The inclination of the shadowband motor was adjusted until the drive shaft angle was within ~0.2 deg of the site latitude (39 deg N). Finally the band was manually adjusted so that the band shadow was centered over the diffuser at each cycle during the entire day. This shadowing adjustment was initially done during installation on October 1, 2002, within 1 h of solar noon, but was also checked throughout routine operation and readjusted if necessary. During routine operation, the internal clock of the instrument was checked against a reference universal time every night via modem line and adjusted so that time error was never larger than 4 s. These procedures enabled accurate sun tracking all day throughout the year

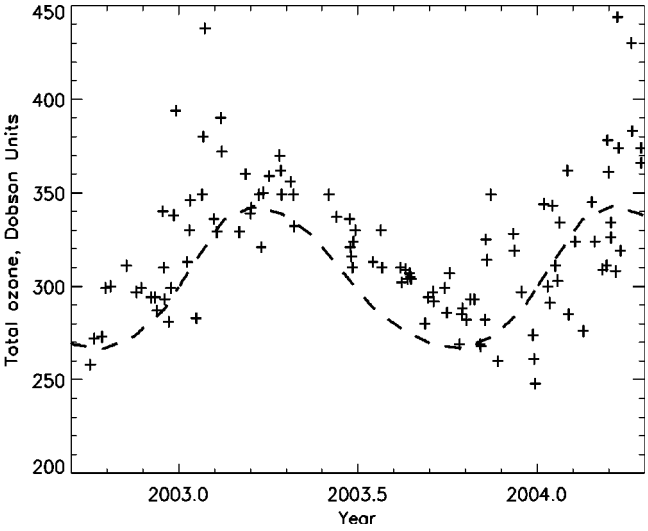

Fig. 2 Brewer daily mean column ozone measurements at GSFC site on cloud-free days in 2002 to 2004 (crosses). Dashed line shows climatological mean ozone values from London et al.[38] assumed in AERONET CIMEL processing.[33,34]

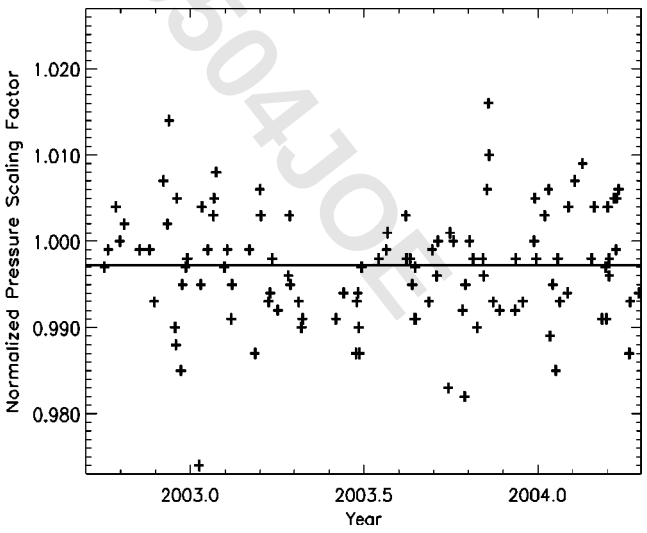

Fig. 3 Daily average pressure measurements normalized to standard 1013.25-mbar pressure. Pressure measurements from USDA UVMRP Beltsville station corrected for altitude differences with NASA GSFC site [~20 m according to global positioning system (GPS) measurements and converted to 2 mbar constant offset]. The annual mean pressure scaling factor was 0.995 with ~3% peak-to-peak variations. Only cloud free days are shown.

Table 1 UV-MFRSR measurement and residual correction errors.

Sources of measured errors in UV-MFRSR 368 nm channel	τ=0.2		τ=0.8	
	θ=30	θ=70	θ=30	θ=70
	Typical measured signal (mV)			
Total, V_T	1300	400	1100	300
Diffuse, V_D	560	300	700	280
Diffuse fraction, D_T	0.43	0.75	0.64	0.93
	Measurementerrors, $\sigma_{\ln V_T}$			
$\Delta \ln V_T$: quantization[1]	0.001	0.003	0.001	0.003
$\Delta \ln V_T$: nighttime bias voltages[2]	0.002	0.007	0.002	0.007
$\Delta \ln V_T$: temperature[3]	0.01	0.01	0.01	0.01
$\Delta \ln V_T$: cosine correction[4]	0.005	0.01	0.005	0.01
$\Delta \ln V_T$: shadowing correction[5]	0.01	0.01	0.01	0.01
Combined measurement error root mean square (rms): $\Delta \ln V_T$	~0.018	~0.02	~0.025	~0.03

[1]Quantization error of the analog voltage signal.

[2]According to the standard deviation of the nighttime bias voltages statistics: mean night time voltage for the 368-nm channel was 2 mV, with standard deviation σ=2.4 mV.

[3]The temperature dependence of nighttime bias voltage was estimated ~2 mV/deg.

[4]Combined error due to the difference between pre- and postdeployment laboratory f_R characterization (Fig. 4) and sky homogeneity assumption in f_D calculation (Sec. 3.2).

[5]Residual error in the excess sky radiance blockage correction.[26,39]

using a good approximation to the solar ephemeris.[26] During ordinary operation the Teflon diffuser was routinely cleaned except for special experimental periods when the diffuser was purposely not cleaned for up to 2 months to investigate the effects of diffuser surface soiling on the instrument's throughput (discussed in Sec. 5).

3.2 *Raw Voltage Corrections*

As described by Harrison et al.,[26] the UV-MFRSR instrument measures total horizontal and diffuse horizontal irradiances in terms of detector voltages. Within the instrument's data logger, the correction for excess sky radiance blockage was first added to the measured diffuse component.[26,39] Next, the direct normal voltage was determined by subtraction of the diffuse component from the total and was normalized by the cosine of the solar zenith angle. The total, diffuse, and direct normal voltages were transferred to the USDA UVMRP center every night via a dedicated modem line for further processing. The data were processed as described in the following few paragraphs. The processing procedures were essentially corrections for nighttime bias voltages and deviation of the instrument's angular response from a perfect cosine dependence.[26,27] Since the internal temperature of the instrument was maintained close to 42 °C, no temperature corrections to the data were deemed necessary. The residual errors of the corrections were treated as random errors and included in the total measured voltage error budget, as explained in Table 1.

Stray currents or voltages generated by the electronics in the absence of light are referred to as the nighttime bias voltages V_{bias}. It is the presence of ac current, and its associated magnetic fields, that creates these bias voltages. When there were ac power failures, and the instrument was running solely on battery power, all V_{bias} values were close to zero ±1 mV. The V_{bias} differs in different channels and could be of a positive or negative value, depending on the sensitivity of that channel's circuit to electronic noise. To correct for this problem, the previous night's V_{bias} were subtracted from the diffuse horizontal voltages by the following procedure: (1) determining the time of the minimum solar elevation during the previous 1 to 3 days, (2) averaging the nighttime bias readings from 1 h prior to 1 h after the time of minimum solar elevation, and (3) subtracting the average V_{bias} from measured diffuse voltage (if more than 1 mV). The typical nighttime V_{bias} was small: at 368 nm, the average V_{bias}=1.7 mV (σ=0.552) compared to the typical daytime diffuse signal ~300 mV (Table 1). The nighttime bias voltage correction was unnecessary for the other components since the direct component was effectively corrected during the subtraction in the data logger and the total horizontal voltage was recalculated as explained below.

Next, angular corrections were applied to the direct and diffuse voltages to compensate for the instrument's angular response deviation from an ideal (cosine) angular response.[26,27,40,41] The cosine correction factor for direct normal voltage $f_R(\theta_0, \varphi)$ was interpolated according to solar zenith θ_0 and azimuth angles, φ at the time of the measurement as described in Ref. 26. The solar azimuth φ (0 to 359 deg) was resolved into the four quadrants, and the f_R was weighted using two scans of the laboratory measured angular responses: one from the south to north (labeled SN), and one from the west to east scan[26,27] (WE). Figure 4 shows the scans at 368 nm as measured at NOAA CUCF Laboratory before and after UV-MFRSR deployment at GSFC. Only predeployment laboratory f_R scans were used to correct the field measurements (shown by symbols in

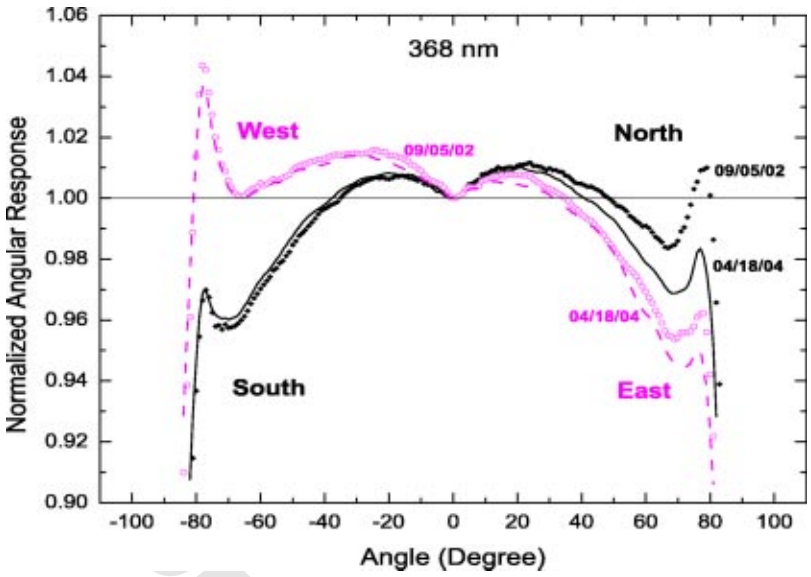

Fig. 4 UV-MFRSR head 271 angular response functions f_R at 368 nm, normalized to the ideal (cosine) angular response ($f_R=1$ for ideal instrument) as measured at NOAA CUCF laboratory before (symbols) and after (lines) deployment at GSFC site. The scans are typically not symmetric and also differ for different channels mainly because the filter/detector assembly of each channel views diffuser cavity at different azimuth angle with respect to the illumination beam.[26,27] Therefore, for each of the seven channels, two sets of measured responses are required: one from the south (on the left, negative angles) to north (on the right, positive angles) scan [labeled SN and shown with filled diamonds (before) and solid line (after)] and one from the west (on the left, negative angles) to east (on the right, positive angles) scan [labeled WE and shown with open circles (before) and dashed lines(after)].

Fig. 4). The postdeployment calibration was used to confirm f_R stability during field deployment. Small f_R drifts were detected only for ''north'' and ''east'' scans (Fig. 4), but were practically negligible for $\theta_0<60$ deg. At larger θ_0 noticeable f_R drift (~2%) had occurred only in the ''north'' illumination direction, which could account for the maximal 0.6% f_R error in summer conditions at GSFC location (latitude=39.03 deg N). The small drift in the ''east'' direction could also account for maximal ~0.5% f_R error in the morning measurements. These possible errors were included in the total error budget in Table 1.

Angular response factors for the diffuse voltages $f_D(\lambda)$ were determined using an isotropic sky assumption.[40,41] The diffuse, nighttime bias-corrected horizontal voltage was divided by the diffuse angular correction factor f_D, which was estimated 0.993 for the 368-nm channel using predeployment f_R scans (and 0.990 using postdeployments f_R scans). Experimental measurements of the actual sky radiance distribution in UV and visible had shown that an isotropic sky radiance assumption by itself underestimates the f_D up to 10% at 500 nm, 6% at 400 nm, 4% at 350 nm, and ~2% at 320 nm, depending on sky inhomogeneity factor.[40] However, the diffuser optics of the instrument used in that study[40] deviated significantly from the ideal cosine response: $f_D(\text{isotropic})\sim 0.88$. On the other hand, the diffuser geometry for the UV-MFRSR instruments was specifically designed to compensate for cosine errors[26,27] so that $f_D(\text{isotropic})\sim 0.99$ at 368 nm for UV-MFRSR 271. Thus, only ~0.5% maximal uncertainty in $f_D(\text{isotropic})$ was assumed at 368 nm due to unaccounted sky radiance inhomogeneity (Table 1). Since the sky radiance is more isotropic at shorter UV wavelengths, the error in $f_D(\text{isotropic})$ gets smaller at shorter wavelengths UV-MFRSR channels.

Finally, the total corrected horizontal voltage V_T was recalculated by summing the cosine corrected direct normal voltage (converted back to horizontal) and the diffuse horizontal voltage corrected for the angular response and the nighttime bias. The whole process can be described using a single correction factor for the total irradiance f_T; $V_T(\text{corrected})=V_T^{\text{Meas}}/f_T$:

$$\frac{1}{f_T}=\frac{1-D_T^{\text{Meas}}}{f_R}+\frac{D_T^{\text{Meas}}-V_{\text{bias}}/V_T^{\text{Meas}}}{f_D(\text{isotropic})}, \tag{1}$$

where D_T^{Meas} is measured (raw) diffuse to total voltage ratio, f_R is normalized direct angular response (Fig. 4), and $f_D(\text{isotropic})\sim 0.99$ at 368 nm. The expected errors in $V_T(\text{corrected})$ already discussed are summarized in Table 1 along with the explanation of their estimates.

The USDA UVMRP reports the corrected voltages, on its website (http://uvb.nrel.colostate.edu/UVB/home_page.html) as ''angular (cosine) corrected data.'' Furthermore, it is these corrected direct normal voltages that were input to the Langley analysis program[28] and operational calculation of τ_a by UVMRP. Alternatively, in our experiment, the corrected voltages were used directly. They were continuously calibrated against a rotating triad of ref-

Table 2 UV-MFRSR spectral band model.[1]

Nominal Band Wavelength[2] (nm)	299.845	305.497	311.575	317.730	325.592	332.654	368.011
	UV-B channels				UV-A channels		
λ_{eff}[3]	300.397	305.726	311.706	317.779	325.687	332.636	367.963
λ_{rad}[4]	300.063	305.313	311.753	317.986	325.808	332.208	367.956
τ_R[5]	1.216	1.128	1.031	0.947	0.854	0.786	0.5105
τ_{O3}[6]	3.335	1.55	0.681	0.292	0.095	0.020	0.00007
τ_a[7]	0.123	0.121	0.118	0.116	0.113	0.111	0.100
$\langle E_{top}\rangle$ (W/m^2 nm)[8]	0.48	0.62	0.72	0.75	0.92	0.98	1.19
$\langle E_{bot}\rangle$ (W/m^2 nm)[9]	0.00004	0.002	0.02	0.05	0.11	0.16	0.35
Transmittance $T_r=\langle E_{bot}\rangle/\langle E_{top}\rangle$	0.0001	0.004	0.03	0.07	0.12	0.16	0.29

[1]Example is given for unit pressure scaling factor, 350-Dobson units (DU) column ozone amount, and aerosol extinction optical thickness 0.1 at 368 nm (Ångström parameter $\alpha=1$). Atmospheric transmittance is calculated for airmass $m=2$ (solar zenith angle 60 deg).

[2]Spectral response functions were measured by CUCF in air (September 2002). All wavelengths are shifted to vacuum wavelength scale.

[3]Channel weighted effective wavelength at the bottom of atmosphere.

[4]Equivalent monochromatic wavelength for direct irradiance at the bottom of atmosphere [Eq. (1)].

[5]Rayleigh scattering coefficients were based on the work by Bates.[42]

[6]The high-spectral-resolution (~0.05-nm) ozone absorption coefficients are based on the laboratory measurements of Bass and Paur.[43]

[7]Nominal aerosol model with $\tau_a(368)=0.1$ and Ångström parameter $\alpha=1$.

[8]Extraterrestrial solar irradiance by high-resolution ATLAS-3 SUSIM measurements (0.05-nm spectral steps) multiplied with interpolated SRF and integrated over bandpass. This gives the band-pass average ETS at the top of atmosphere $\langle E_{top}\rangle$ (W/m^2 nm) with diffuser oriented toward the sun at 1 AU.

[9]Bandpass average direct normal irradiance, $\langle E_{bot}\rangle$ (W/m^2 nm) that would be measured in each UV-MFRSR channel at the bottom of atmosphere with diffuser oriented toward the sun at 1 AU.

erence AERONET sun photometers (CIMELs), as described in the next section.

3.3 *UV-MFRSR On-Site Calibration Technique*

Assuming that the UV-MFRSRs radiometric sensitivity (gain) remains constant (e.g., doubling the irradiance results in doubling the voltage), one only needs to know V_0 (instrument voltage for direct solar flux extrapolated to the top of the atmosphere) to derive the atmospheric transmittance directly from the voltage measurements. The same V_0 was applied to direct and diffuse voltages, since both are measured by the same diffuser/filter/detector combination.[26] Therefore, our on-site calibration strategy consisted in continuous on-site V_0 estimation and included the following steps:

1. Calculate spectral direct atmospheric transmittance $T_R(\lambda)$ given colocated near simultaneous auxiliary measurements of aerosol extinction optical thickness τ_a (interpolated from AERONET CIMEL direct sun measurements as discussed later), pressure scaling factor P (surface pressure normalized to 1013.25 mbar) to correct Rayleigh optical thickness τ_R and τ_a as well as column ozone to calculate gaseous (ozone) absorption optical thickness, τ_{O3} (Table 2 and Fig. 5):

$$T_R(\lambda)=\exp\{-m[\tau_a(\lambda)+\tau_R(\lambda)P+\tau_{O3}(\lambda)]\}. \quad (2)$$

The relative airmass factor m was approximated as secant of the solar zenith angle, θ_0, for $\theta_0<75$ deg (corrections to m were necessary at shorter wavelengths or larger solar zenith angles[29]).

2. Develop a UV-MFRSR spectral band model to calculate equivalent transmittance in each channel, T_R(channel), by numerically integrating the product of spectral atmospheric transmittance $T_R(\lambda)$, measured instrument spectral response function, $F(\lambda)$, and spectral solar flux E_0 [ATLAS-3 solar UV spectral irradiance monitor (SUSIM), 0.05-nm spectral steps] over bandwidth for each individual measurement:

$$T_R(\text{channel})=\frac{\int_{\lambda_{min}}^{\lambda_{max}}E_0(\lambda)F(\lambda)T_R(\lambda)d\lambda}{\int_{\lambda_{min}}^{\lambda_{max}}E_0(\lambda)F(\lambda)\mathrm{d}\lambda}. \quad (3)$$

In Eq. (3) the denominator represents the absolute bandpass average solar flux E_{top} that would be measured by the UV-MFRSR at the top of the atmosphere [λ_{min} and λ_{max} are channel cutoff wavelengths $F(\lambda)$], while the numerator represents the attenuated solar flux measured at the surface E_{bot} with the same instrument. The parameters of the spectral band model developed for UV-MFRSR 271 are summarized in Table 2 for a nominal aerosol model and shown in Fig. 5 for the 332-nm channel.

3. Calculate logarithm of the calibration constant $\ln(V_0)$ for each individual measurement of direct-normal

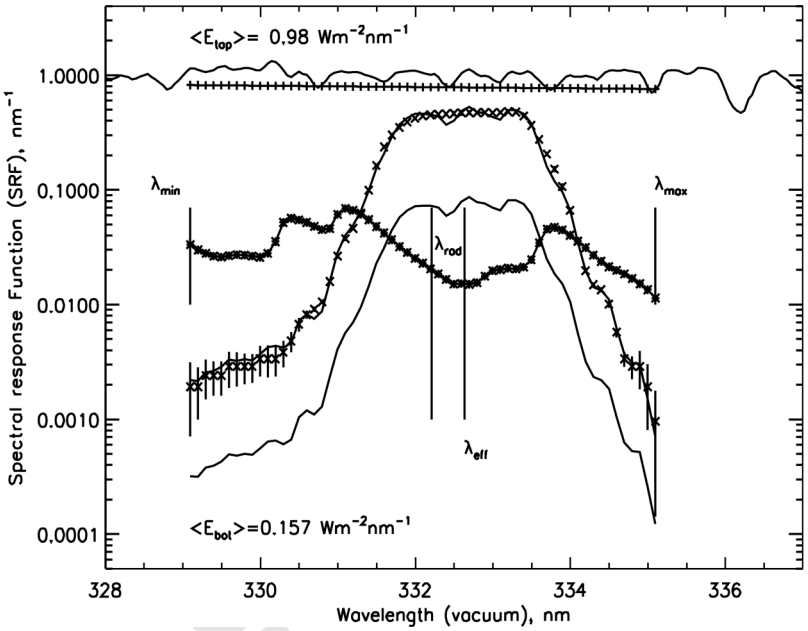

Fig. 5 Example of high-resolution spectral band model for 332-nm channel of UV-MFRSR 271. Spectral response functions (SRFs) were measured at CUCF in September 2002 before instrument's deployment at GSFC site, normalized to unit spectral integral and shifted to vacuum wavelength scale ("X" symbols with error bars). Also shown are extraterrestrial spectral solar irradiance (ETS, top curve, taken from SUSIM ATLAS-3 measurements), Rayleigh optical thickness τ_R (plus symbols), ozone optical thickness, τ_{O3} (stars, for 350-DU ozone amount and weighted temperature −45 °C), spectral direct irradiance multiplied with SRF and ETS at the top of atmosphere and with transmittance, $T_R(\lambda)$ at the surface (assuming unit surface pressure scaling factor, aerosol optical thickness 0.1 at 368 nm and Angström parameter=1) along with bandpass average values at the top and bottom of atmosphere. The channel effective wavelength λ_{eff} and radiatively equivalent wavelength λ_{rad} are shown as vertical bars. The spectral band model parameters for all UV-MFRSR channels are summarized in Table 2.

voltage V_n using precalculated T_R(channel) for this measurement:

$$\ln(V_0)=\ln(V_n)-\ln[T_R(\text{channel})]. \quad (4)$$

We note that absolute values of the solar flux are not important for calculating T_R(channel) and calibration factor from Eqs. (3) and (4).

4. Obtain daily average calibration factor, $\langle \ln(V_0)\rangle$ and standard deviation, $\sigma_{\ln(V_0)}$; iteratively remove the outlier measurements [outside of $3\sigma_{\ln(V_0)}$] and recalculate $\langle \ln(V_0)\rangle$ (see Fig. 7 in Sec. 4).
5. Calculate bandpass effective wavelength λ_{eff} for each channel:

$$\lambda_{\text{eff}}=\frac{\int_{\lambda_{\min}}^{\lambda_{\max}}\lambda E_0(\lambda)F(\lambda)T_R(\lambda)\mathrm{d}\lambda}{\int_{\lambda_{\min}}^{\lambda_{\max}}E_0(\lambda)F(\lambda)T_R(\lambda)\mathrm{d}\lambda}. \quad (5)$$

6. Calculate spectral-band radiatively equivalent wavelength λ_{rad} by solving Eq. (6) for λ_{rad} for each individual measurement:

$$T_R(\lambda_{\text{rad}})=T_R(\text{channel}). \quad (6)$$

To obtain a unique solution for λ_{rad} only values falling in the interval ($\lambda_{\text{eff}}-0.5$ nm, $\lambda_{\text{eff}}+0.5$ nm) were retained.

7. Calculate aerosol optical thickness $\tau_a(\lambda_{\text{rad}})$ using measured direct-normal voltage V_n daily average calibration $\langle \ln(V_0)\rangle$, and subtracting Rayleigh and ozone contributions. Save λ_{rad}, $\tau_a(\lambda_{\text{rad}})$, $\tau_{O3}(\lambda_{\text{rad}})$, and $\tau_R(\lambda_{\text{rad}})$ to correctly partition total atmospheric optical thickness between different atmospheric processes in calculating diffuse irradiance component from monochromatic radiative transfer equation (described in the second part of the paper[36]).
8. Calculate measured total and diffuse atmospheric transmittances by normalizing corresponding voltages (discussed in Sec. 3.2) by $\exp[\langle \ln(V_0)\rangle]$.

Using λ_{rad}, Eqs. (2) to (4) could be rewritten in a compact linear form suitable for Langley regression:

$$\ln(V_0)=\ln(V_n)+m[\tau_a(\lambda_{\text{rad}})+\tau_R(\lambda_{\text{rad}})P+\tau_{O3}(\lambda_{\text{rad}})]. \quad (7)$$

To derive V_0 from either Eq. (4) or Eq. (7) the aerosol extinction optical thickness τ_a should be interpolated or extrapolated to any given λ within UV-MFRSR spectral bandbass using AERONET discrete spectral τ_a measurements.[33,34,44] In practice, we use AERONET interpolated/extrapolated $\tau_a(\lambda)$ at high spectral resolution to calculate spectral atmospheric transmittance within each

Table 3 Calibration changes between Mauna Loa calibrations for each of the three reference AERONET CIMEL instruments at GSFC site in 2002–2004.[1]

Inst. Number	Start date at GSFC	End date at GSFC	$\ln(V_{0\ predeployment}/V_{0\ postdeployment})$[1]		Central Wavelength		Rayleigh Subtraction	
			340	380	340	380	340	380
94	12/16/03	03/25/04	−0.015[8]	0.001[8]	339.9	379.4	0.706	0.445
	05/13/03	06/17/03	−0.016[5]	0.016[5]	339.9	379.4	0.706	0.445
	02/21/03	03/13/03	−0.010[3]	0.004[3]	339.9	379.4	0.706	0.445
	12/18/02	02/03/03	−0.010[3]	0.004[3]	339.9	379.4	0.706	0.445
89	10/17/03	12/15/03	N/A[9]	N/A[9]	339.9	380.1	0.706	0.442
	06/18/03	07/24/03	−0.022[6]	−0.017[6]	340.0	379.4	0.705	0.445
	02/04/03	02/20/03	0.005[2]	0.004[2]	340.0	379.4	0.705	0.445
	09/28/02	12/17/02	0.005[2]	0.004[2]	340.0	379.4	0.705	0.445
101	07/25/03	10/16/03	−0.007[7]	−0.015[7]	340.3	380.2	0.706	0.445
	03/14/03	05/12/03	−0.009[4]	0.003[4]	340.3	380.2	0.703	0.441

[1]Multiple (~5 to 20) morning Langley calibrations at Mauna Loa observatory (MLO) were done for AERONET reference instruments before and after deployment at GSFC. The drift between Mauna Loa calibrations is defined as $\ln(V_{0,predeployment}/V_{0,postdeployment})$. The Rayleigh optical depth subtraction in 340- and 380-nm channels was required for atmospheric pressure correction and is shown for each instrument.

[2]CIMEL 89 predeployment calibration on 09/09/2002, postdeployment calibration on 05/22/2003. Small increases in V_0 with time (<0.5% between MLO calibrations) may possibly be due to uncertainty in the determination of V_0.

[3]CIMEL 94 predeployment calibration on 11/15/2002, postdeployment calibration on 04/11/2003.

[4]CIMEL 101 predeployment calibration on 02/12/2003, postdeployment calibration on 07/02/2003.

[5]CIMEL 94 predeployment calibration on 04/11/2003, postdeployment calibration on 08/25/2003.

[6]CIMEL 89 predeployment calibration on 05/22/2003; postdeployment calibration on 10/06/2003.

[7]CIMEL 101 predeployment calibration on 07/02/2003; postdeployment calibration on 12/09/2003.

[8]CIMEL 94 predeployment calibration on 11/16/2003, postdeployment calibration on 06/14/2004.

[9]CIMEL 89 postdeployment calibration not available due to mechanical modification of sensor filter wheel. The predeployment calibration on 10/06/2004 was used for this period.

bandpass and numerically evaluate the spectral integral in Eqs. (3) to (5). The $\tau_a(\lambda)$ interpolation/extrapolation technique is described in the next section.

3.4 *Spectral Extrapolation/Interpolation of AERONET Direct-Sun Measurements*

The AERONET reference sunphotometers (CIMELs) were calibrated every 3 to 6 months at the high altitude (~3 km) Mauna Loa Observatory, Hawaii, using the sun a source[33,34,44] (Table 3). The calibration uncertainty in τ_a for the reference CIMELs was estimated better than 0.002 to 0.005 in the visible,[34] but up to 0.01 in the UV (Ref. 44). One of the reasons for higher uncertainty in UV was that in the operational AERONET processing there was no adjustment of Rayleigh optical depth for departure from mean surface pressure.[33,34,44] Since day-to-day variations in pressure reach 3% even for cloud free days (Fig. 3), the standard AERONET τ_a data were corrected in the UV (340 and 380 nm) for the actual atmospheric pressure at the time of measurement:

$$\Delta\tau_a(\lambda,t)=\tau_R(\lambda)[1-P(t)/P_A]. \quad (8)$$

In Eq. (8) τ_R is AERONET standard Rayleigh optical thickness subtraction for specific instrument and channel (Table 3), adjusted to the mean site pressure scaling factor P_A ($P_A=0.994$ at GSFC); and $P(t)$ is the true pressure scaling factor at time of measurement (surface pressure normalized to 1013.25 mbar). The maximum $\Delta\tau_a$ correction caused by observed atmospheric pressure variations at our site (Fig. 3) was ~0.01 at 340 nm, while at 380 nm, the correction was half of that amount and proportionately less at visible wavelengths. Additionally, in AERONET computation of τ_a for 340, 500, and 675 nm, ozone optical depth was also subtracted from total optical depth using climatological mean ozone values.[38] Because of the small ozone absorption at these wavelengths, departures from climatological values by 50% (which are very large fluctuations) would result in additional uncertainty in computed τ_a of only ~0.004 at 340 nm and 0.0045 at 500 nm (longer AERONET wavelengths were not used in calibration). Typical departures would be less than half this magnitude (see Fig. 2). Therefore, the combined error in CIMEL τ_a was estimated ~0.002–0.01 in the visible for a single CIMEL reference instrument[44] at GSFC. Taking into account differences between reference CIMEL instruments in UV, the uncertainty increases[44] to 0.02.

The AERONET τ_a measurements at 340, 380, 440, and 500 nm were extrapolated or interpolated to the UV-MFRSR wavelengths using a least squares quadratic fit in log-log space[44] (Fig. 6). The linear extrapolation in log-log space (dashed curve in Fig. 6) was also used assuming that the Ångstrom parameter did not change in the UV-A. Although this assumption does not hold for large wavelength spans[44] (~100 nm), both methods provided practically identical results in the UV-A spectral region between 325 and 368 nm. Therefore, the wavelength extrapolation error

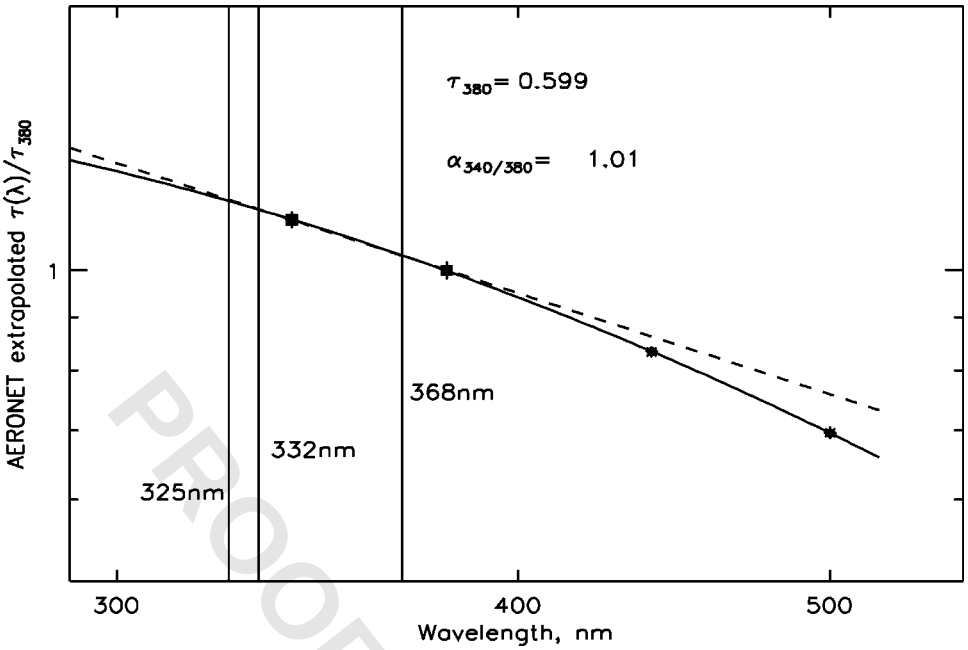

Fig. 6 AERONET direct sun aerosol extinction optical thickness τ_a at 340, 380, 440, and 500 nm normalized by τ_a (380 nm) (symbols with error bars). Extrapolation using quadratic least-squares fit of $\ln(\tau_a)$ versus $\ln(\lambda)$ is shown as a solid line, and linear extrapolation of (τ_a) versus $\ln(\lambda)$ from 340- and 380-nm measurements is shown as a dashed line. The UV-MFRSR 325-, 332-, and 368-nm channels are shown as vertical bars. The typical differences between the extrapolation methods at these channels were less than 0.005.

was considered insignificant for calibration purposes at UV-MFRSR UV-A channels.

Using sensitivity modeling assuming maximal NO_2 loadings reported at GSFC location,[45] the NO_2 absorption effect was also found insignificant for the purpose of calibration transfer.

4 UV-MFRSR Daily V_0 Calibration Results

Figure 7 shows examples of daily V_0 calibration transfer results at 368 nm for cloud-free days with high (top panel) and low (lower panel) aerosol loadings. Standard deviation of individual 3-min V_0 data, $\sigma_{\ln V_0}$, provides an overall measure of atmospheric and instrumental variability on a given day and is directly related to the uncertainty in derived individual τ_a values. On the clearest days at GSFC the scatter in V_0 was quite small ($\sigma_{\ln V_0} \sim 0.006$ for $\tau_a \sim 0.1$, lower panel), but the scatter increased on days with high turbidity ($\sigma_{\ln V_0} \sim 0.03$ for $\tau_{\text{ext}} \sim 0.6$, upper panel). Calculating daily means of individual V_0 values reduces the effect of random errors for transferring the AERONET calibration by the square root of the number of available measurements. Typically there were ~60 daily V_0 estimates in winter compared to ~200 in summer, therefore, random error in estimating daily mean $\langle V_0 \rangle$ value (shown as a horizontal line in Fig. 7) was reduced by a factor 8 to 20. The effect of random errors was further reduced by removing outlier measurements [with $\ln(V_0)$ outside of $\pm 3\sigma_{\ln V_0}$ of the $\langle \ln(V_0) \rangle$] and iteratively recalculating $\langle V_0 \rangle$. The V_0 outliers on apparently cloud free days could be explained in part by the fact that the heavy rf environment of the CIMEL transmitters might be influencing the data logger. They could be also due to real short-term fluctuations in τ_a not resolved by the 15-min CIMEL measurements,[33–35,37] but captured in 3-min UV-MFRSR data. We found that removing less than 5% of outliers typically reduces $\sigma_{\ln V_0}$ by half on both clear and turbid days (in Fig. 7 $\sigma_{\ln V_0}$ are shown for three iterations).

Examining diurnal trends in V_0 data provides insight into possible systematic calibration errors and yields a tool for checking consistency between AERONET-CIMEL τ_a and UV-MFRSR voltage measurements. For perfect measurements, V_0 should remain constant during the day regardless of any changes in atmospheric transmission, solar elevation and azimuth (at least for $\theta_0 < 75$ deg, additional corrections to m were necessary at shorter wavelengths or larger solar zenith angles[29]). Therefore, any systematic residual errors in UV-MFRSR cosine or shadowing corrections would manifest themselves as systematic $\ln(V_0)$ changes with solar zenith angle. On the other hand, any constant error in AERONET extrapolated τ_a would produce systematic errors in $\ln(V_0)$ that are proportional to the airmass factor, m [see Eq. (7)], and would result in a diurnal pattern in $\ln(V_0)$ with systematic increase or decrease at high m, depending on the sign of the τ_a error. For example, a small systematic decrease in $\ln(V_0) \sim 0.015$ can be seen on March 14, 2002 (Fig. 7, lower panel), in early morning and late evening at $m \sim 5$. Assuming that all this decrease is due to the error in extrapolation of τ_a, the upper limit of this error could be estimated: $\Delta\tau_{\text{ext}} \sim 0.015/5 = 0.003$ (assuming the error remains constant during that day) that is within

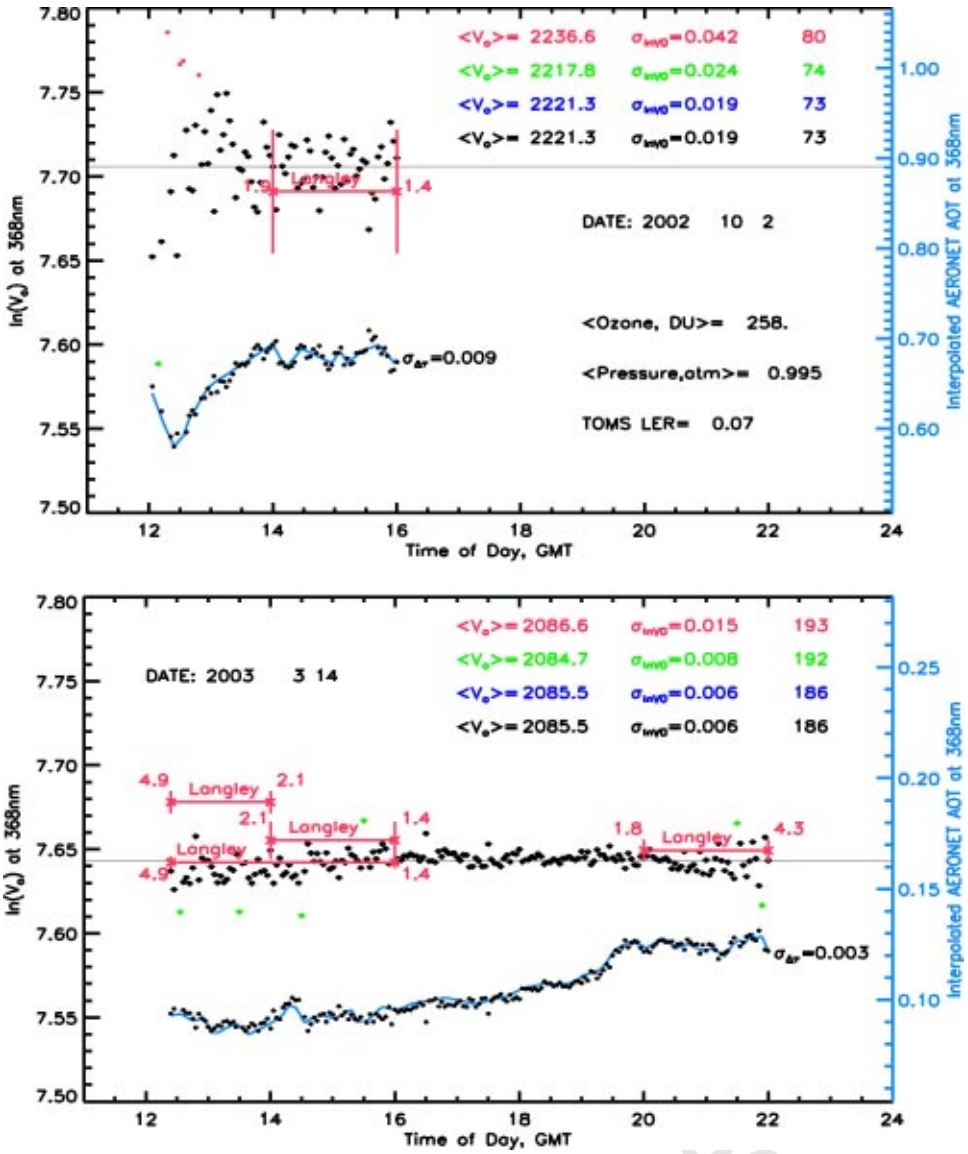

Fig. 7 Daily V_0 calibration results on cloud-free days with high (top) and low (bottom) aerosol loading. Points represent individual V_0 estimates and the horizontal line represents daily average $\langle V_0 \rangle$ value after removing the outlier UV-MFRSR measurements outside of $\pm 3\sigma_{\ln V_0}$ (three iterations are shown in different colors). The 2-h Langley plot intercepts are represented as red horizontal lines with $1\sigma_{\ln V_0}$ error bars and initial and final airmass values used in regression. Interpolated AERONET direct-sun τ_a is shown as a blue line, and calculated UV-MFRSR τ_a are shown as black crosses for each 3-min measurement (with scale on the right). Daily root mean square (rms) differences between the AERONET and the UV-MFRSR τ_{ext} are also shown on the right to the τ_{ext} curves.

uncertainty of AERONET τ_a measurements. To summarize, a day-long calibration period enables a better estimate of possible systematic errors in the overall calibration procedure while reducing the effect of random errors by the square root of the number of retained measurements.

There was still a possibility that different systematic errors could compensate each other in such a way as to cancel any observable diurnal dependence in $\ln(V_0)$, while still producing a bias in daily mean $\langle V_0 \rangle$. Therefore, an independent on-site calibration method was used to cross-validate AERONET calibration procedure. In perfectly stable atmospheric conditions, the Langley plot calibration method can provide a very good check on the measurements, spectral band model and $\langle V_0 \rangle$ calibrations.[28,29] Standard Langley technique regresses $\ln(V_n)$ versus m, so $\ln(V_0)$ is obtained as the zero airmass intercept of a linear regression model given by Eq. (7). The method does not require knowledge of the absolute atmospheric transmittance, beyond the stability requirement. Therefore, the Langley technique was optimized by adjusting the time interval used in the regression of Eq. (7) to ensure maximum possible stability of τ_a during Langley calibration.

Figure 7 shows that optimized Langley $\ln(V_0)$ values were indeed within 0.01 to 0.02 of the AERONET $\ln(V_0)$ results (1σ error bars), when $\tau_a \sim$ const. The comparisons,

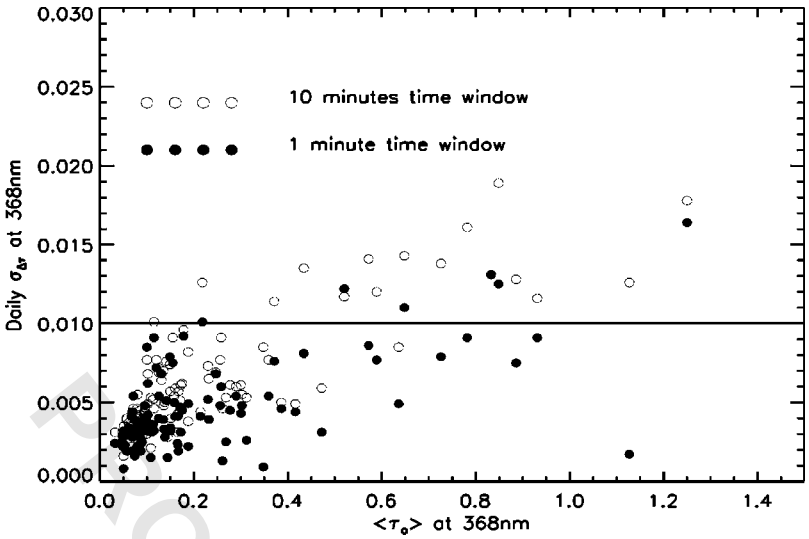

Fig. 8 Daily aerosol extinction optical thickness τ_a rms differences between UV-MFRSR and AERONET CIMEL measurements, $\sigma_{\Delta\tau}$ at 368 nm shown as a function of daily mean τ_a. The comparison time window was reduced from 10 min (open circles) to 1 min (black circles) to show effects of short-term atmospheric variability on τ_a comparisons.

although somewhat subjective, provide crucial evidence of the consistency between AERONET-CIMEL and Langley UV-MFRSR calibrations, except for outlier measurements of less that 5% of the total (see Fig. 7).

As a final consistency check, the aerosol optical thickness τ_a was calculated for each individual 3-min UV-MFRSR V_n measurement (except outlier measurements of less than 5% of the total, see Fig. 7) using daily mean $\langle V_0 \rangle$ value and compared with AERONET extrapolated τ_a. Both instruments showed consistent τ_a results with no obvious bias (Fig. 7) and small scatter (Fig. 8). Daily rms differences $\sigma_{\Delta\tau}$ were <0.005 on clear days ($\tau_a<0.2$ at 368 nm), but increased systematically with τ_a reaching $\sigma_{\Delta\tau}\sim 0.02$ on turbid days. The increase in $\sigma_{\Delta\tau}$ with increase in atmospheric turbidity was attributed to short-term atmospheric τ_a variability, not resolved by 15-min AERONET observations, but captured by 3-min UV-MFRSR measurements.

When the time window for individual τ_a comparisons was reduced to 1 min the $\sigma_{\Delta\tau}$ decreased, most noticeably on turbid days despite the fact that there were less measurements to average. Part of the remaining τ_a differences could still be attributed to even shorter atmospheric fluctuations with periods less than 1 min. The Smirnov et al. cloud screening algorithm[37] allows a range of 0.02 in min-max τ_a over a 1-min time interval from three measurements taken 30 s apart, and still be classified as cloud free. At higher τ_a the allowable range is $(0.03\times\tau_a)$ over the 1-min interval. This allowable range is largely due to the real 1-min variability of τ_a. Similar analysis at shorter UV wavelengths (325 and 332 nm) revealed a slight increase in $\sigma_{\Delta\tau}$ ($\sigma_{\Delta\tau}<0.02$) relative to 368-nm data, which could be attributed to a larger wavelength extrapolation interval, while overall comparison results were similar. Analysis has shown that the UV-MFRSR, when intercalibrated against an AERONET sun photometer on the same day, was proven reliable to retrieve τ_a. However, such calibrations should be repeated daily due to systematic day-to-day changes in UV-MFRSR throughput as discussed in the next section.

5 Long-Term Changes in UV-MFRSR V_0 Calibration

Comparisons of aerosol extinction optical thickness provided an independent check of both instrument's calibration and enabled relative tracking of the UV-MFRSR throughput changes in all channels by repeating the comparisons on clear days. Using such calibrations, it was found that the UV-MFRSR had relatively good day to day calibration reproducibility in summer [$\pm 2\%$ in $\langle V_0(368)\rangle$], but larger than expected V_0 changes in the fall and winter seasons. The changes included periods of systematic day-to-day V_0 decline for extended periods alternating with step jump changes after major precipitation periods (rain or snow). Figure 9 shows day-to-day changes in daily V_0 values in the 368-nm channel, normalized to sun to earth distance r(AU): $\ln(r^2V_0)$ and allowing a 10-min time window between CIMEL and UV-MFRSR measurements. The normalization removed the V_0 seasonal cycle due to changes in extraterrestrial solar irradiance with sun to earth distance and emphasized changes in the instrument throughput. Initial V_0 estimation after deployment (day 1 calibration) was performed on a clear hazy morning on October 2, 2002 ($\tau_a\sim 0.7$, see Fig. 7), and yielded the highest $V_0(368)$ value $\ln(r^2V_0)>=7.7$, followed by steady V_0 decline at a rate of $\sim 0.15\%$/day for more than 2 months with minimal value $\ln(r^2V_0)=7.59$ reached on December 16. The first upward step jump ($+0.04$) had occurred between December 17, 2002 [$\langle\ln(r^2V_0)\rangle=7.59$] and next clear sky calibration on December 21 [$\ln(r^2V_0)=7.63$] and was probably caused by diffuser cleaning. After that event, $\ln(r^2V_0)$ continued to decrease at the same rate until January 27, 2003, when the largest upward step jump ($+0.07$) had occurred with the next clear-sky calibration on February 5 [$\ln(r^2V_0)=7.64$].

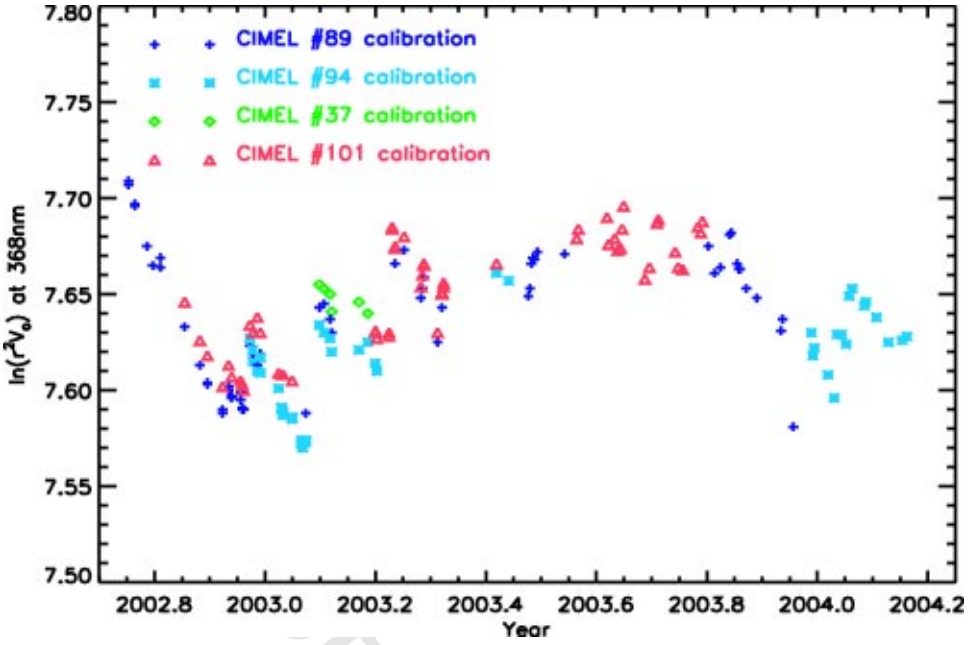

Fig. 9 UV-MFRSR daily calibration results ($\langle V_0 \rangle$ at 368 nm, normalized to the sun-to-earth distance) using different AERONET reference CIMEL instruments, that were themselves calibrated every 3 to 6 months at high altitude (~3 km) MLO, Hawaii, using the sun as a source[33,34,42] (Table 3).

The third step jump (+0.04) had occurred between March 23 and 25, 2003. After that, calibration stabilized until the fall of 2003, when an instrument's throughput decline started again resembling the behavior in 2002. The calibrations were repeated using different reference CIMEL instruments, but the differences in $\ln(r^2V_0)$ from using different CIMELs as calibration sources were small (0.01 to 0.02, Fig. 9). Changing the allowable time window between individual measurements from 10 to 1 min resulted in even smaller changes in $\ln(r^2V_0)$ (~0.01, not shown). Therefore, these two calibration transfer error sources combined could not explain more than 10% of the seasonal changes in the V_0, and so were attributed to the real changes in the throughput of the UV-MFRSR instrument.

The V_0 changes were highly correlated in all three wavelength channels, although the seasonal cycle was stronger at shorter UV wavelengths (332 and 325 nm) (Fig. 10). In addition, radiometric calibrations of the unit were performed at the CUCF laboratory[30] before and after deployment at GSFC site. The percentage changes from the predeployment radiometric calibration on day 246, 2002, to the postdeployment calibration on day 107, 2004, were much smaller (−4.08, −2.83, and −4.5% at 325, 332, and 368 nm, respectively) than V_0 seasonal variations and can be explained by the filter degradations. These findings imply that the seasonal cycle was caused either by the changes in the sensitivity of the whole instrument (not individual filters or detectors) or by the seasonal changes in environmental conditions affecting in a systematic way the UV-MFRSR performance and/or on-site calibration procedure. Although the particular cause(s) for V_0 seasonal cycle remains unknown, we considered several possible explanations.

The seasonal dependence of the ambient air temperature plus direct radiant sun heating could potentially affect calibration of any field instrument. However, the UV-MFRSR internal head temperature was maintained above the average temperature at the GSFC site and constantly monitored throughout deployment ($\langle T \rangle = 41.7°C$, $\sigma_T = 0.22°C$). The internal temperature gradients could have had some effect on calibration, but those were not obvious via diurnal V_0 dependence (between morning and noon hours) (Fig. 7). The temperature gradient inside the diffuser material could have also contributed to the calibration: many different types of Teflon show an increasing transmission of 2 to 3%, when the temperature (of the Teflon) is increasing[46,47] between ~10 over about 20°C.

The sealing of the optical head and elevated and stable internal temperature helped maintain low internal humidity, which was monitored via a color indicator (turns from dark blue to pink with an increase in internal humidity).[26] Therefore, seasonal changes in ambient temperature and humidity were deemed unlikely as a major source of the observed seasonal calibration cycle. To rule out potential solar zenith effects, the calibrations were repeated restricting individual measurements to those with solar zenith angles larger than 50 deg, so that solar illumination conditions were the same in winter and summer. Despite the substantial reduction in number of individual calibration measurements in summer months, daily V_0 results had changed less than 1% in all spectral channels.

The systematic day-to-day decline in normalized V_0 for extended periods could have been attributed to cumulative diffuser soiling by aerosols, which reduced diffuser transmission for all spectral channels.[26] To confirm this hypothesis a test of diffuser contamination was performed by not cleaning the diffuser for 2 months after January 14, 2004, and then cleaning it thoroughly on the clear day March 14, 2004, near noon, when irradiance level was high. A +4% upward step jump was recorded in measured voltages in all

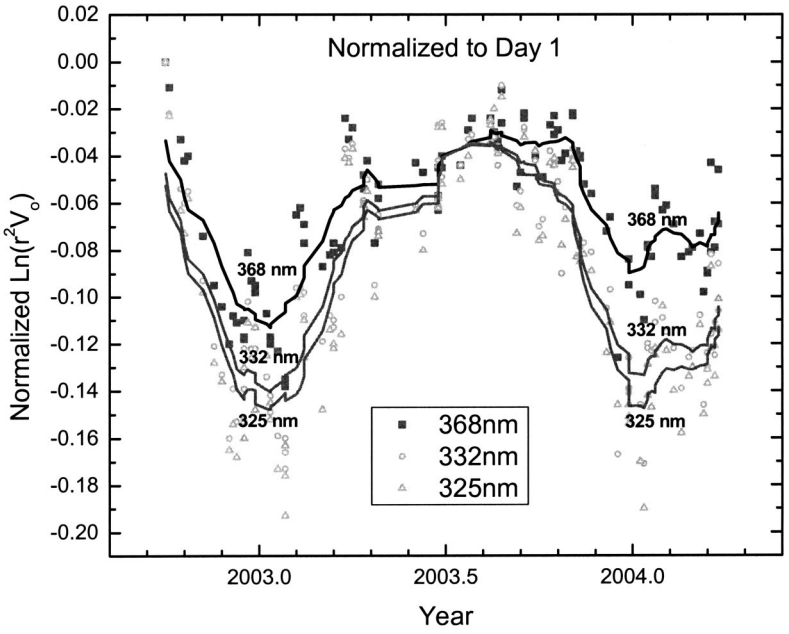

Fig. 10 UV-MFRSR normalized V_0 calibration results in three longer wavelength channels V_0 (368 nm) (black squares), V_0 (332 nm) (open circles), and V_0 (325 nm) (open triangles). In each channel, the V_0 calibrations were normalized to day 1 calibration to emphasize the spectral dependence of the long-term calibration drift. The lines are 10-day running means of corresponding normalized daily V_0s. An increment of 0.01 corresponds to 1% change in V_0.

three channels immediately after cleaning. Therefore, the step jump changes in $\ln(r^2V_0)$ can be explained in part by Teflon diffuser manual cleanings and/or self-cleanings after major precipitation events (rain or snow). However, the cleanings alone were not sufficient to explain neither stronger long-term V_0 seasonal cycle ($\sim$10% at 368 nm and 15% at shorter channels) nor the large spectral differences in fall and winter season (Fig. 10).

To rule out any unknown calibration transfer errors, both objective[28,29] and time-window optimized Langley (described in Sec. 4 and Fig. 7) calibration techniques were used to confirm long-term changes in UV-MFRSR throughput observed with AERONET calibrations. Figure 11 compares the calibration results by three methods. Both on-site Langley techniques produce significant day-to-day variations, but with the variations for the objective technique (not shown) much larger. Therefore, only the optimized time-window Langley technique tends to confirm the V_0 time dependence seen from AERONET calibration, while the objective technique produces a relatively large range of values with no clear trend. The largest differences between objective Langley and AERONET V_0 were observed on days with monotonic τ_a changes during Langley calibration period. It was shown, using 3-min τ_a data, that a monotonic increase in τ_a by 15% during typical 2-h operational Langley observation period (3 to 1.5 airmass) resulted in systematic V_0 underestimation by $>$10%. Consequently, on days with monotonically decreasing τ_a, V_0 was systematically overestimated. Using long-term time smoothing technique of daily V_0s, from the UVMRP operational Langley analysis[28,29] (solid curve in Fig. 11) reduces the maximal errors, but at the expense of missing seasonal cycle in normalized V_0 observed with AERONET calibrations. As a result, using only the operational Langley time-interpolated curve could produce errors in derived τ_a up to 0.05 at 368 nm in worst conditions ($\Delta\tau_a \sim \Delta V_0/m$ in winter noon times with airmass $m=2$), while maximum τ_a (368 nm) errors in summer were only $\sim$0.02. On the other hand, using calibration transfer from a well-maintained and calibrated sun photometer reduces $\tau_a(368)$ errors further to less than $\sim$0.01 in all conditions (Fig. 8).

The causes for V_0 seasonal cycle remain unknown, and must be confirmed with independent UV-MFRSR units. If confirmed, one possible hypothesis would be that aerosols are substantially more absorbing in UV in the fall to winter season than in summer at GSFC site. The reported high values of aerosol single scattering albedo ($\omega \sim 0.98$) at GSFC site were all in fact obtained in summer, when aerosol extinction optical thickness was[35] larger than 0.4 at 440 nm.

To the extent that aerosol absorption at 440 nm could serve as a proxy for UV absorption, these measurements[35] are in agreement with relatively good V_0 reproducibility in summer ($\pm$2%). The deposition of weakly absorbing aerosols does not substantially affect the transmission of an already optically thick diffuser.[26] However, it appears that in dry fall and winter seasons, the absorption of aerosol residual deposited on the surface of the Teflon diffuser becomes much stronger than in summer. This aerosol residual embedded into Teflon material was not completely removed with manual cleanings, but was gradually bleached in the spring to summer period, when solar irradiance was high. In addition, the spectral dependence of the aerosol UV absorption should be opposite to that found in summer[35]

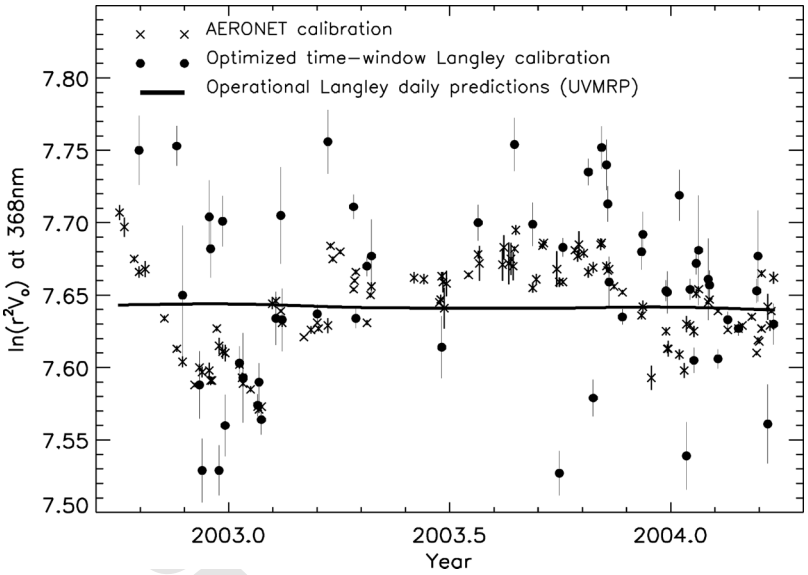

Fig. 11 UV-MFRSR 368-nm channel on-site Langley calibrations versus AERONET calibration at GSFC site. AERONET calibrations are the same as in Figs. 9 and 10 and are shown for comparisons with UVMRP operational daily predicted calibrations (solid line) and time window optimized 2-h on-site Langley calibrations (black circles with error bars). The UVMRP operational calibrations were based on modified objective Langley technique[28,29] and morning airmass range 1.5 to 3. All calibrations were normalized to the average sun-to-earth distance.

to explain enhanced attenuation of the shorter UV channels (325 and 332 nm) compared to the 368-nm channel (Fig. 10). It was previously hypothesized that absorption by organic carbon[48] or nitrated and aromatic aerosol components[5] could be responsible for enhanced UV absorption.

6 Conclusions

A new method of on-site UV-MFRSR calibration was developed using colocated direct sun AERONET/CIMEL τ_a measurements. The AERONET τ_a was interpolated or extrapolated to UV-MFRSR wavelengths and measurement intervals and used as input to the UV-MFRSR spectral band model along with column ozone and surface pressure measurements to estimate zero air mass voltages V_0. The method does not require stability of τ_a and enables independent V_0 estimations for every 3-min measurement in each spectral channel. Daily average $\langle V_0 \rangle$ estimates were obtained for cloud-free conditions and compared with the on-site Langley technique. On the clearest stable days, both calibration techniques were consistent.

Daily mean $\langle V_0 \rangle$ values were used to calculate τ_a for individual 3-min UV-MFRSR measurements ($\sim$5% outlier data rejection). These results compared well with interpolated AERONET τ_a measurements [at 368-nm daily rms differences in τ_a were within 0.01 (1σ) for $\tau_{\text{ext}} < 0.4$ and within $0.015(1\sigma)$ for $\tau_{\text{ext}} < 1.2$]. Therefore, the UV-MFRSR, when intercalibrated against an AERONET sunphotometer on the same day was proven reliable to retrieve τ_a. However, the calibrations should be repeated daily due to systematic day-to-day changes in UV-MFRSR throughput. The changes included periods of systematic day to day $\langle V_0 \rangle$ decline for time periods of over a month [we identified four such periods with $\sim$0.15%/day decline in $V_0(368\,\text{nm})$] alternated with step jumps changes after major precipitation periods (rain or snow). The $\langle V_0 \rangle$ day-to-day changes were highly correlated in three longer wavelength UV-MFRSR channels (325, 332, 368 nm), and possibly result from diffuser contamination and cleanings. Such V_0 changes necessitate Teflon diffuser cleanings of stand-alone UV-MFRSR field instruments at least two times weekly or adding a quartz dome, which is less likely to absorb dirt particles.

The essential advantage of the shadowband technique is that $\langle V_0 \rangle$ calibration obtained for direct-sun voltage can be applied to diffuse and total voltages to obtain total and diffuse atmospheric transmittances. These transmittances in combination with accurate τ_a data provide an essential foundation for the aerosol column absorption retrievals described in the second part of this paper.[36]

Acknowledgments

We thank Kathleen Lantz and Patrick Disterhoft from Cooperative Institute for Research in Environmental Science, National Oceanic and Atmospheric Administration, Boulder, Colorado, and Lee Harrison, Mario Blumthaler, and Germar Bernhard for in depth discussions about UV-MFRSR performance and calibrations. We are grateful to Alexander Smirnov and Ilya Slutsker for help with AERONET data and Tommy Taylor for careful reading the manuscript. We acknowledge NASA's Office of Earth Science (Code YS) for continued support through the TOMS Science Team and thank two reviewers for suggesting improvements to the paper.

References

1. O. Wild, X. Zhu, and M. J. Prather, "Fast-J: accurate simulation of in- and below-cloud photolysis in tropospheric chemical models," *J. Atmos. Chem.* **37**, 245–282 (2000).

2. M. Z. Jacobson, ''Studying the effects of aerosols on vertical photolysis rate coefficient and temperature profiles over an urban airshed,'' *J. Geophys. Res.* **103**, 10593–10604 (1998).
3. R. R. Dickerson, S. Kondragunta, G. Stenchikov, K. L. Civerolo, B. G. Doddridge, and B. N. Holben, ''The impact of aerosols on solar Ultraviolet radiation and photochemical smog,'' *Science* **28**, 827–830 (1997).
4. S. Madronich, ''UV radiation in the natural and perturbed atmosphere,'' in *Environmental Effects of Ultraviolet (UV) Radiation*, pp. 17–69, Lewis Publisher, Boca Raton, FL (1993).
5. M. Z. Jacobson, ''Isolating nitrated and aromatic aerosols and nitrated aromatic gases as sources of ultraviolet light absorption,'' *J. Geophys. Res.* **104**, 3527–3542 (1999).
6. N. A. Krotkov, P. K. Bhartia, J. R. Herman, V. Fioletov, and J. Kerr, ''Satellite estimation of spectral surface UV irradiance in the presence of tropospheric aerosols 1. cloud-free case,'' *J. Geophys. Res.* **103**(D8), 8779–8793 (1998).
7. A. Kylling, A. F. Bais, M. Blumthaler, J. Schreder, C. S. Zerefos, and E. Kosmidis, ''Effect of aerosols on solar UV irradiances during the photochemical activity and solar ultraviolet radiation campaign,'' *J. Geophys. Res.* **103**, 26051–26060 (1998).
8. B. N. Wenny, J. S. Schafer, J. J. DeLuisi, V. K. Saxena, W. F. Barnard, I. V. Petropavlovskikh, and A. J. Vergamini, ''A study of regional aerosol radiative properties and effects on ultraviolet-B radiation,'' *J. Geophys. Res.* **103**(D14), 17083–17097 (1998).
9. J. Reuder and H. Schwander, ''Aerosol effects on UV radiation in nonurban regions,'' *J. Geophys. Res.* **104**, 4065–4077 (1999).
10. J. R. Herman, N. Krotkov, E. Celarier, D. Larko, and G. Labow, ''The distribution of UV radiation at the earth's surface from TOMS measured UV-backscattered radiances,'' *J. Geophys. Res.* **104**, 12059–12076 (1999).
11. B. N. Wenny, V. K. Saxena, and J. E. Frederick, ''Aerosol optical depth measurements and their impact on surface levels of ultraviolet-B radiation,'' *J. Geophys. Res.* **106**, 17311–17319 (2001).
12. J. L. Petters, V. K. Saxena, J. R. Slusser, B. N. Wenny, and S. Madronich, ''Aerosol single scattering albedo retrieved from measurements of surface UV irradiance and a radiative transfer model,'' *J. Geophys. Res.* **108**(D9), 4288 (2003); (doi:10.1029/2002JD002360).
13. M. A. Wetzel, G. E. Shaw, J. R. Slusser, R. D. Borys, and C. F. Cahill, ''Physical, chemical, and ultraviolet radiative characteristics of aerosol in central Alaska,'' *J. Geophys. Res.* **108**(D14), 4418 (2003); (doi:10.1029/2002JD003208).
14. N. A. Krotkov, J. R. Herman, P. K. Bhartia, C. Seftor, A. Arola, J. Kurola, S. Kalliscota, P. Taalas, and I. Geogdzhaev, ''Version 2 TOMS UV algorithm: problems and enhancements,'' *Opt. Eng.* **41**(12), 3028–3039 (2002).
15. N. A. Krotkov, J. R. Herman, P. K. Bhartia, C. Seftor, A. Arola, J. Kaurola, P. Taalas, I. Geogdzhaev, and A. Vasilkov, *OMI Surface UV Irradiance Algorithm*, P. Stammes, Ed., vol. 3, ATBD-OMI_03, (http://eospso.gsfc.nasa.gov/eos_homepage/for_scientists/atbd/docs/OMI/ATBD-OMI-03.pdf).
16. V. Fioletov, J. B. Kerr, D. I. Wardle, N. Krotkov, and J. R. Herman, ''Comparison of Brewer ultraviolet irradiance measurements with total ozone mapping spectrometer satellite retrievals,'' *Opt. Eng.* **41**(12), 3051–3061 (2002).
17. J. B. Kerr, G. Seckmeyer, A. F. Bais, G. Bernhard, M. Blumthaler, S. B. Diaz, N. Krotkov, D. Lubin, R. L. McKenzie, A. A. Sabziparvar, and J. Verdebout, ''Surface ultraviolet radiation: past and future,'' Chap. 5 in *Scientific Assesment of Ozone Depletion: 2002, Global Ozone Research and Monitoring Project*, Report N 47, World Meteorological Organization, Geneva (2003).
18. G. A. d'Almeida, P. Koepke, and E. P. Shettle, *Atmospheric Aerosols: Global Climatology and Radiative Characteristics*, A. Deepak Publ., Hampton, VA (1991).
19. I. N. Sokolik and O. B. Toon, ''Incorporation of mineralogical composition into models of the radiative properties of mineral aerosol from UV to IR wavelengths,'' *J. Geophys. Res.* **104**(D8), 9423–9444 (1999).
20. S. C. Alfaro, S. Lafton, J. L. Rajot, P. Formenti, A. Gaudichet, and M. Maille, ''Iron oxides and light absorption by pure desert dust: an experimental study,'' *J. Geophys. Res.* **109**(D0), 8208 (2004); (doi:10.1029/2003JD004374).
21. J. T. Twitty and J. A. Weinman, ''Radiative properties of carbonaceous aerosols,'' *J. Appl. Meteorol.* **10**, 725–731 (1975).
22. H. Horvath, ''Atmospheric light absorption—a review,'' *Atmos. Environ.* **27A**, 293–317 (1993).
23. R. W. Bergstrom, P. B. Russell, and P. Hignett, ''Wavelength dependence of the absorption of black carbon particles: predictions and results from the TARFOX experiment and implications for the aerosol single scattering albedo,'' *J. Atmos. Sci.* **59**, 567–577 (2002).
24. D. S. Bigelov, J. R. Slusser, A. F. Beaubien, and J. R. Gibson, ''The USDA ultraviolet radiation monitoring program,'' *Bull. Am. Meteorol. Soc.* **79**, 601–615 (1998).
25. J. A. Kaye, B. B. Hicks, E. C. Weatherhead, C. S. Long, and J. R. Slusser, ''US Interagency UV Monitoring Program established and operating,'' *EOS (Wash. D.C.)* **80**(10), 114–116 (1999).
26. L. Harrison, J. Michalsky, and J. Berndt, ''Automated multi-filter rotating shadowband radiometer: an instrument for optical depth and radiation measurements,'' *Appl. Opt.* **33**, 5118–5125 (1994).
27. J. J. Michalsky, L. C. Harrison, and W. E. Berkheiser III, ''Cosine response characteristics of some radiometric and photometric sensors,'' *Sol. Energy* **54**(6), 397–402 (1995).
28. L. Harrison and J. Michalsky, ''Objective algorithms for the retrieval of optical depths from ground-based measurements,'' *Appl. Opt.* **33**, 5126–5132 (1994).
29. J. R. Slusser, J. H. Gibson, D. Kolinski, P. Disterhoft, K. Lantz, and A. F. Beabien, ''Langley method of calibrating UV filter radiometer,'' *J. Geophys. Res.* **105**, 4841–4849 (2000).
30. K. Lantz, P. Disterhoft et al., ''The 1997 North American interagency intercomparison of ultraviolet spectroradiometers including narrowband filter radiometers,'' *J. Res. Natl. Inst. Stand. Technol.* **107**, 19–62 (2002).
31. J. Slusser et al., ''Comparison of column ozone retrievals by use of an UV multifilter rotating shadow-band radiometer with those from Brewer and Dobson spectrophotometers,'' *Appl. Opt.* **38**, 1543–1551 (1999).
32. W. J. Gao, J. R. Slusser, J. H. Gibson, G. Scott, D. S. Bigelow, J. Kerr, and B. McArthur, ''Direct-Sun column ozone retrieval by the Ultraviolet Multi-filter Rotating Shadow-band Radiometer and comparison with those from Brewer and Dobson spectrophotometers,'' *Appl. Opt.* **40**(19), 3149–3155 (2001).
33. B. N. Holben et al., ''AERONET—a federated instrument network and data archive for aerosol characterization,'' *Remote Sens. Environ.* **66**, 1–16 (1998).
34. B. N. Holben et al., ''An emerging ground-based aerosol climatology: aerosol optical depth from AERONET,'' *J. Geophys. Res.* **106**, 12067–12097 (2001).
35. O. Dubovik, B. Holben, T. Eck, A. Smirnov, Y. J. Kaufman, M. D. King, D. Tanre, and I. Slutsker, ''Variability of absorption and optical properties of key aerosol types observed in worldwide locations,'' *J. Atmos. Sci.* **59**, 590–608 (2002).
36. N. Krotkov, P. K. Bhartia, J. Herman, J. Slusser, G. Scott, G. Labow, A. P. Vasilkov, T. Eck, O. Dubovik, and B. Holben, ''Aerosol ultraviolet absorption experiment (2002 to 2004): 2. Absorption optical thickness, retractive indix, and single scattering albedo,'' *Opt. Eng. (this issue).*
37. A. Smirnov, B. N. Holben, T. F. Eck, O. Dubovik, and I. Slutsker, ''Cloud screening and quality control algorithms for the AERONET data base,'' *Remote Sens. Environ.* **73**(3), 337–349 (2000).
38. J. London, R. D. Bojkov, S. Oltmans, and J. I. Kelly, ''Atlas of the global distribution of total ozone July 1957–June 1967,'' NCAR Tech. Note 133+STR, NCAR, CO (1976).
39. M. L. Wesely, ''Simplified techniques to study components of solar radiation under haze and clouds,'' *J. Appl. Meteorol.* **21**, 373–383 (1982).
40. J. Grobner, M. Blumthaler, and W. Ambach, ''Experimental investigation of spectral global irradiance measurement errors due to a non ideal cosine response,'' *Geophys. Res. Lett.* **23**(18), 2493–2496 (1996).
41. Leszscynski et al., ''Erythemal weighted radiometers,'' *Photochem. Photobiol.* **67**(2), 212–221 (1998).
42. D. R. Bates, ''Rayleigh scattering by air,'' *Planet. Space Sci.* **32**, 785–790 (1984).
43. A. M. Bass and R. J. Paur, ''The ultraviolet cross-sections of ozone, I, measurements,'' in *Atmospheric Ozone, in Ozone Symposium (1984:Halkidiki, Greece): Atmospheric Ozone*, C. Z. Zeferos and A. Ghaz, Eds., pp. 606–616, D. Reidel, Hingham, MA (1985).
44. T. F. Eck, B. N. Holben, J. S. Reid, O. Dubovik, A. Smirnov, N. T. O'Neill, I. Slutsker, and S. Kinne, ''Wavelength dependence of the optical depth of biomass burning, urban and desert dust aerosols,'' *J. Geophys. Res.* **104**, 31333–31350 (1999).
45. A. N. Rublev, N. E. Chubarova, A. N. Trotsenko, and G. I. Gorchakov, ''Determination of NO_2 column amounts from AERONET data,'' *Atmos. Oceanic Phys.* **40**, 54–67 (2004).
46. J. Gröbner, M. Blumthaler, and J. Schreder, ''Characterization report of the traveling standard B5503,'' EUR 20699, European Commission (2003); available at http://lap.physics.auth.gr/qasume/.
47. R. McKenzie, J. Badosa, M. Kotkamp, and P. Johnston, ''Effects of the temperature dependence in PTFE diffusers on observed UV irradiances,'' submitted for publication.
48. T. W. Kirchstetter, T. Novakov, and P. Hobbs, ''Evidence that the spectral dependence of light absorption by aerosols is affected by organic carbon,'' *J. Geophys. Res.* **109**, D21208 (2004); (doi:10.1029/2004JD004999).

Nickolay Krotkov received a BS degree in physics and MS degree in remote sensing in 1985 from the Moscow Institute of Physics and Technology, Russia. He received his PhD in oceanography (physics and mathematics) in 1990 from the P. P. Shirshov Institute of Oceanology, Russian Academy of Sciences, for research on using polarization properties of light in oceanic remote sensing. He joined NASA, Goddard Space Flight Center in 1993 where he worked on applications of satellite data, such as mapping surface UV irradiance and generation of UV volcanic eruption data products from the NASA Total Ozone Mapping Spectrometer (TOMS) missions. His main field of research is radiative transfer modeling, satellite and ground based UV data analysis, and inversions. He is currently a senior research scientist with GEST Center University of Maryland Baltimore County.

Pawan K. Bhartia received his PhD in physics and MS degree in computer science in 1977 from Purdue University, West Lafayette, Indiana. Since then he has been associated with NASA's Goddard Space Flight Center (GSFC) in Greenbelt, Maryland. Between 1977 and 1991 he worked with several private companies, including Systems and Applied Sciences Corporation STX, SAR, Interferometrics, and TRW on NASA contracts. Since October 1991, he has been a NASA employee. Currently he is the head of the Atmospheric Chemistry and Dynamics Branch at GSFC. He is also the project scientist of NASA's Total Ozone Mapping Spectrometer (TOMS) satellite mission and the U.S. science team leader of the Ozone Monitoring Instrument (OMI)—a joint project between NASA and The Netherlands. He has over 50 publications in UV remote sensing of the Earth from satellites, dealing principally with the measurement of the Earth's ozone layer. He is a member of the American Geophysical Union.

Jay Herman received his BS degree in 1959 from Clarkson, and MS in 1963, and PhD in 1965 in physics and aeronomy from Pennsylvania State University. He joined NASA, Goddard Space Flight Center, first with a National Academy of Sciences postdoctoral appointment and then as a staff scientist. He has worked in a number of fields including chemical modeling of the Earth and planetary atmospheres, radiative transfer, satellite data studies of ozone, clouds, surface reflectivity, and UV radiation in the atmosphere and oceans. He currently is project scientist on the Deep Space Climate Observatory at the Lagrange-1 observing point. He is also principal investigator on the Earth UV radiation project. He is a long-term member of the American Geophysical Union.

James Slusser studied physics at Western Michigan University and received his bachelor's degree in 1977 and his master's degree in 1980. The next nine years were spent in Chicago, Illinois, where he was the undergraduate physics laboratory director at Loyola University. Later he worked as a design engineer for Atlas Electric Devices, serving as a project manager for an ultraviolet outdoor radiometer and temperature probe for weathering chambers. In 1989 he returned to school to study atmospheric science and radiative transfer at the University of Alaska at Fairbanks. His dissertation involved measuring stratospheric nitrogen dioxide and exploring its relationship to ozone abundances. After earning his PhD in 1994 he spent three months at Lauder, New Zealand, doing trace gases analysis using the zenith sky spectroscopy. He then took up a position as a research associate at the Center for Atmospheric Science at Cambridge University in England, where he investigated the effects of volcanic aerosols on nitrogen dioxide and ozone abundances in Antarctica. In 1996 he became a research scientist at the USDA UV-B Monitoring and Research Program at Colorado State University, and in 1999 he became program director. His current research interests include improving the calibration accuracy and precision of UV measurements and retrievals of trace gas column abundances and aerosol properties. He has authored or co-authored more than 25 papers. He is a member of the AGU, AMS, and SPIE, and served as an associate editor of the *Journal of Geophysical Research*.

Gordon Labow received a BS degree from Virginia Tech in 1986 and joined NASA's Goddard Space Flight Center Solar Maximum Mission team that same year. He worked on increasing our understanding of the processes that create solar flares and methods of flare prediction. In 1992 he began to work with the Total Ozone Mapping Spectrometer (TOMS) team and has experience with the instrumentation and algorithmic methods used for detection of ozone, as well as the statistical techniques used for the calculation of ozone trends. He has experience working on ground-based instrumentation, such as spectrometers, radiometers, ozonesondes, and others, used to detect trace gases such as ozone, SO_2, NO_2 as well as aerosols. He is currently a senior scientist with Science Systems & Applications Inc. of Lanham, Maryland.

Gwendolyn Scott received a BA degree in biology (with a chemistry minor) from the University of Evansville in 1971, and a BS degree in computer science from Colorado State University (CSU) in 1998. She has been employed at CSU's Natural Resource Ecology Laboratory for 26 years: in the laboratory, performing chemical analyses from 1974 to 1982; in data management for the National Atmospheric Deposition Program (NADP) from 1983 to 1994; and, in software development for the USDA UV-B Monitoring and Research Program since 1998.

George Janson received a BS degree in chemical engineering from Syracuse University in 1975. He joined the USDA UV-B Monitoring and Research Program in 1996 where he works as a field engineer servicing network instruments and analyzing the long-term stability of the various instruments.

Thomas F. Eck received a BS degree in meteorology from Rutgers University in 1977 and an MS degree in meteorology from the University of Maryland, College Park, in 1982 where his major interests were in micrometeorology and remote sensing. In 1981 be began work at Goddard Space Flight Center and has continued through to the present. He is currently a research scientist with the GEST Center, University of Maryland, Baltimore County, where he carries out instrument calibration and deployment, field experimentation, data analysis, and scientific research within the global Aerosol Robotic Network (AERONET) project. He has authored and co-authored over 65 papers with recent emphasis on studies of the optical properties of atmospheric aerosols, especially from biomass burning and fossil fuel combustion, and the attenuation of solar flux by aerosols.

Brent Holben received his MS degree from Colorado State University, Fort Collins, in 1976, specializing in biometeorology and remote sensing. He is currently a research scientist at NASA's Goddard Space Flight Center, Greenbelt, Maryland. He was a staff scientist with the University of Puerto Rico, Puerto Rico Nuclear Center investigating mesoscale radiation balance in the Luquillo Experimental Forest until 1978 when he joined the GSFC. He has published research on remote sensing of vegetation dynamics, atmospheric corrections to remotely sensed data, and more recently, aerosol optical properties. He is the project leader of the ground-based aerosol characterization program AERONET, initiating and guiding its development since 1992.

PROOF COPY 509504JOE